

Long Term Variability of O VII Line Intensity toward the Lockman Hole

Observed with Suzaku from 2006 to 2011

Hiroshi YOSHITAKE *, Kazuhiro SAKAI, Kazuhisa MITSUDA, Noriko Y. YAMASAKI,
Yoh TAKEI, and Ryo YAMAMOTO

*Institute of Space and Astronautical Science, Japan Aerospace Exploration Agency (ISAS/JAXA),
3-1-1 Yoshinodai, Chuo, Sagamihara, Kanagawa 229-8510
sakai@astro.isas.jaxa.jp*

(Received ; accepted)

Abstract

Long-term time variabilities of the O VII (0.57 keV) emission in the soft X-ray diffuse background were studied using six Suzaku annual observations of blank sky towards the Lockman Hole made from 2006 to 2011. After time intervals in which the emission was enhanced on time scales of a few tens of ks were removed, the O VII intensity was found to be constant from 2006 to 2009 within the 90% statistical errors. The intensity in 2010 and 2011 was higher by 2–3 LU ($= \text{photons s}^{-1} \text{cm}^{-2} \text{sr}^{-1}$) than the earlier values. The most plausible origin of the fast variable component is Solar wind charge exchange (SWCX). The intensity increase is not positively correlated with the proton flux at the L1 point. Since all the observations were made in the same season of a year, the variation cannot be explained by parallax of the SWCX induced X-ray emission from the Heliosphere. We consider that it is related to the geometrical change of slow and fast solar wind structures associated with the 11 year solar activity. The observed variation was compared with that expected from the SWCX induced X-ray emission model.

Key words: X-rays: diffuse background — X-rays: solar wind charge exchange

1. Introduction

The charge exchange process of solar wind ions with neutrals (SWCX) is considered to contribute to the diffuse X-ray background, especially at energies under 1 keV (Koutroumpa

* Present Address is Central Research Laboratory, Hitachi, Ltd., 1-280, Higashi-Koigakubo, Kokubunji, Tokyo 185-8601

et al. 2006). When solar wind ions interact with neutral atoms (mainly H and He), electrons bound in the neutral are transferred to the excited state of the ion, and move to the ground state by emitting X-rays corresponding to the de-excitation energy. Thus the SWCX consists of emission lines, among which the O VII triplet at 0.57 keV is the most prominent and has been observed with X-ray CCD spectrometers on board Chandra, XMM-Newton and Suzaku (Snowden et al. 2004, Fujimoto et al. 2007).

The SWCX-induced diffuse emissions are considered to arise from collisions with neutrals of two different origins. One is the Earth’s geocorona, thus the emission is called “geocoronal SWCX”. According to Østgaard et al. (2003), the geocorona extends with a scale height of $\sim 8.2 R_E$ (earth radii). The other source is atoms of the local interstellar medium (LISM) flowing into the interplanetary space (heliosphere) due to the relative motion of the solar system against the LISM. The heliosphere extends up to ~ 100 AU from the Sun (Lallement et al. 2005), and the emission is called “heliospheric SWCX”.

The contribution of the geocoronal SWCX to the ROSAT All Sky Survey (RASS) 3/4 keV band map was pointed out by Cox (1998), as an enhancement characterized by variability of timescales of a few tens ks to a few days. XMM discovered strong line emissions correlated with the solar wind conditions around the Earth (Snowden et al. 2004). Careful analysis might be able to remove this variable emission from the other X-ray diffuse emission (eg. Yoshino et al. 2009). The general contribution of the heliospheric SWCX has been also debated and demonstrated in several cases (Koutroumpa et al. 2007, Koutroumpa et al. 2011). In particular, Koutroumpa et al. (2007) showed that several observed variations on short or medium time scale can be interpreted to be of the heliospheric SWCX origin.

If the heliospheric SWCX actually contributes to a certain amount of the soft X-ray background, long term emission variations related to the 11-year solar cycle and the inhomogeneity of the interstellar neutral distributions around the Sun are expected. Large variations are mainly expected because of the anisotropic slow/fast solar wind distributions in the solar corona (McComas et al. 2008). Due to the difference in plasma temperature, the O^{+7} and O^{+8} ionization fractions of the slow solar wind (higher temperature) are much larger than those of the fast solar wind. Conversely, the ionization fractions of oxygen ions with ionization state lower than O^{+7} are higher in the fast solar wind. During the solar minimum phase, the slow wind is restricted to within a low heliocentric ecliptic latitude area $|\beta| \lesssim 20^\circ$, and the fast wind widely extends from the polar regions (McComas et al. 2008). On the other hand, the slow wind covers almost the whole solar corona during the maximum phase. For this reason, the heliospheric SWCX-induced emission at high ecliptic latitudes is expected to depend on the long term (11-year) solar activity.

Koutroumpa et al. (2006) calculated all sky emission maps of the heliospheric SWCX induced O VII and O VIII lines on the basis of averaged, minimum and maximum solar activity in Solar Cycle 22. They obtained different O VII and O VIII maps with different solar activity

levels, especially toward the high ecliptic latitudes. According to these model simulations, O VII at higher ecliptic latitudes may be enhanced by 1–2 Line Unit (LU = photons s⁻¹cm⁻²sr⁻¹) at solar maximum relative to minimum from the same observing site along the Earth orbit.

Table 1. Log of the Suzaku Lockman Hole observations.

ID	Start / End date (UT) YYMMDD hh:mm:ss	Exposure (ks)		Screening		Pointing		Roll angle
		total*	screened [†]	1 [‡]	2 [§]	R. A.	Dec.	
LH06	060517 17:44:06 / 060519 19:03:18	80.4	32.5	✓		162°.937	57°.256	281°.872
LH07	070503 23:12:08 / 070506 02:00:19	96.1	56.7		✓	162°.937	57°.258	319°.511
LH08	080518 11:07:29 / 080520 01:16:14	83.4	58.4			162°.937	57°.255	281°.530
LH09	090612 07:17:40 / 090614 01:31:21	92.8	63.8			162°.938	57°.255	281°.530
LH10	100611 07:29:06 / 100613 01:59:22	78.0	50.0	✓		162°.937	57°.251	279°.887
LH11	110504 17:46:34 / 110505 18:25:20	42.3	19.4		✓	162°.920	57°.251	305°.984

* Total exposure of the XIS1 after the standard screening.

[†] Screened exposure extracted when COR2 > 8 GV c⁻¹ and screened by the criteria 1 and 2 (next 2 columns).

[‡] Effect of the geocoronal SWCX induced emission was removed (see §3.1).

[§] Contamination of the neutral O I K α emission was removed (see §3.2).

The purpose of this paper is to investigate the variabilities of the heliospheric SWCX induced O VII line at high ecliptic latitudes, related to the long term solar cycle of ~ 11 years. To avoid the direction dependence of heliospheric SWCX, we must use a set of observations looking toward the same direction. We also need to note that parallax also produces variations, since the distributions of interstellar neutrals in the heliosphere are quite anisotropic (Pepino et al. 2004). We thus need to use those observations made at the same period of time in each year. In addition, it is required to remove time intervals during which the O VII intensity is enhanced over \sim tens of ks, since this indicates enhancement by geocoronal SWCX.

We analyzed O VII and O VIII line intensities toward the Lockman Hole (in the high ecliptic latitude area at $\beta = 45.2^\circ$) with Suzaku (Mitsuda et al. 2007), observed annually from 2006 to 2011. This interval covers about half a Solar Cycle headed from the solar minimum phase at the end of Cycle 23 to the maximum of Cycle 24. This is the first time that the energy spectra from a blank field region, with strictly fixed line of sight and observation configuration, have been compared. If significant differences of the oxygen line intensity still exist, these differences will indicate the long term variability of the heliospheric SWCX induced emission.

In this paper, the stated error ranges show 90% confidence level from the center value, and the vertical error bars in the figures indicate $\pm 1\sigma$ level unless otherwise noted.

2. Observations

Suzaku has annually observed the Lockman Hole (hereafter LH) direction $(\alpha, \delta)/(\ell, b) = (162^\circ.94, 57^\circ.25)/(149^\circ.71, 53^\circ.21)$ since 2006 as a calibration target for the Hard X-ray Detector (HXD). This field is characterized by very low hydrogen column density; $N_{\text{H}} = 5.6 \times 10^{19} \text{ cm}^{-2}$ (Dickey & Lockman 1990, and Hasinger et al. 1993), or $5.8 \times 10^{19} \text{ cm}^{-2}$ (Kalberla et al. 2005). Details of the observations are summarized in Table 1. From this point forth we will refer to the individual observations by using the LH acronym and the corresponding year as listed in the first column of Table 1. Although all observations faced in the same pointing direction within $2'$, the roll angles were different by up to $\sim 40^\circ$ (the fields of view differ by $\sim 20\%$). We use the data of the X-ray Imaging Spectrometer (XIS) on-board Suzaku (Koyama et al. 2007) ver.2.0, 2.0, 2.2, 2.4, 2.5, and 2.5 processed for LH06, LH07, LH08, LH09, LH10, and LH11 respectively. Their energy gain corrections were performed by using `xispi` with the latest makepi file `ae_xi1_makepi_20110621.fits` in CALDB. All XIS data sets were observed with the normal clocking and the 3×3 or 5×5 editing mode. The Spaced-row Charge Injection (SCI) was adopted except for the LH06 observation. The observation LH06 was also analyzed in Yoshino et al. (2009), and our result is consistent with theirs (see the details below).

3. Data Screening

We start from the XIS1 cleaned event files that are processed with standard data screening criteria. To avoid high energy particle penetration due to the Earth's magnetic field, we extracted the data when Cut Off Rigidity (COR2) was larger than $8 \text{ GV } c^{-1}$. Two bright sources whose flux was larger than $1.0 \times 10^{-14} \text{ erg cm}^{-2} \text{ s}^{-1}$ in the $0.5 - 2.0 \text{ keV}$ band were removed by circles with diameters $3'.0$ and $4'.0$ centered at $(\alpha = 162^\circ.811, \delta = 57^\circ.271)$ and $(163^\circ.005, 57^\circ.178)$.

After the data were screened with the above criteria, we additionally removed the intervals when geocoronal SWCX-induced lines and the neutral O I $K\alpha$ line in the Earth's atmosphere were enhanced (screening procedures were described in §3.1 and §3.2). Table 1 shows the exposures of the total cleaned events and the screened ones, and what screening was applied in each observation.

3.1. Removal of the Geocoronal SWCX X-ray Emission

The time scale of geocoronal SWCX variations is about tens of msec to a few days (Snowden et al. 2004; Fujimoto et al. 2007). Therefore, we can assume that when variations reach a minimum intensity during each observation the spectrum is the least contaminated by geocoronal SWCX. The intensity of the geocoronal SWCX-induced line depends on the product of the neutral density in the atmosphere and the solar wind ion flux. A typical scale height of the geocoronal neutrals is $\sim 8.2R_{\text{E}}$ from the Earth's surface (Østgaard et al. 2003), and the

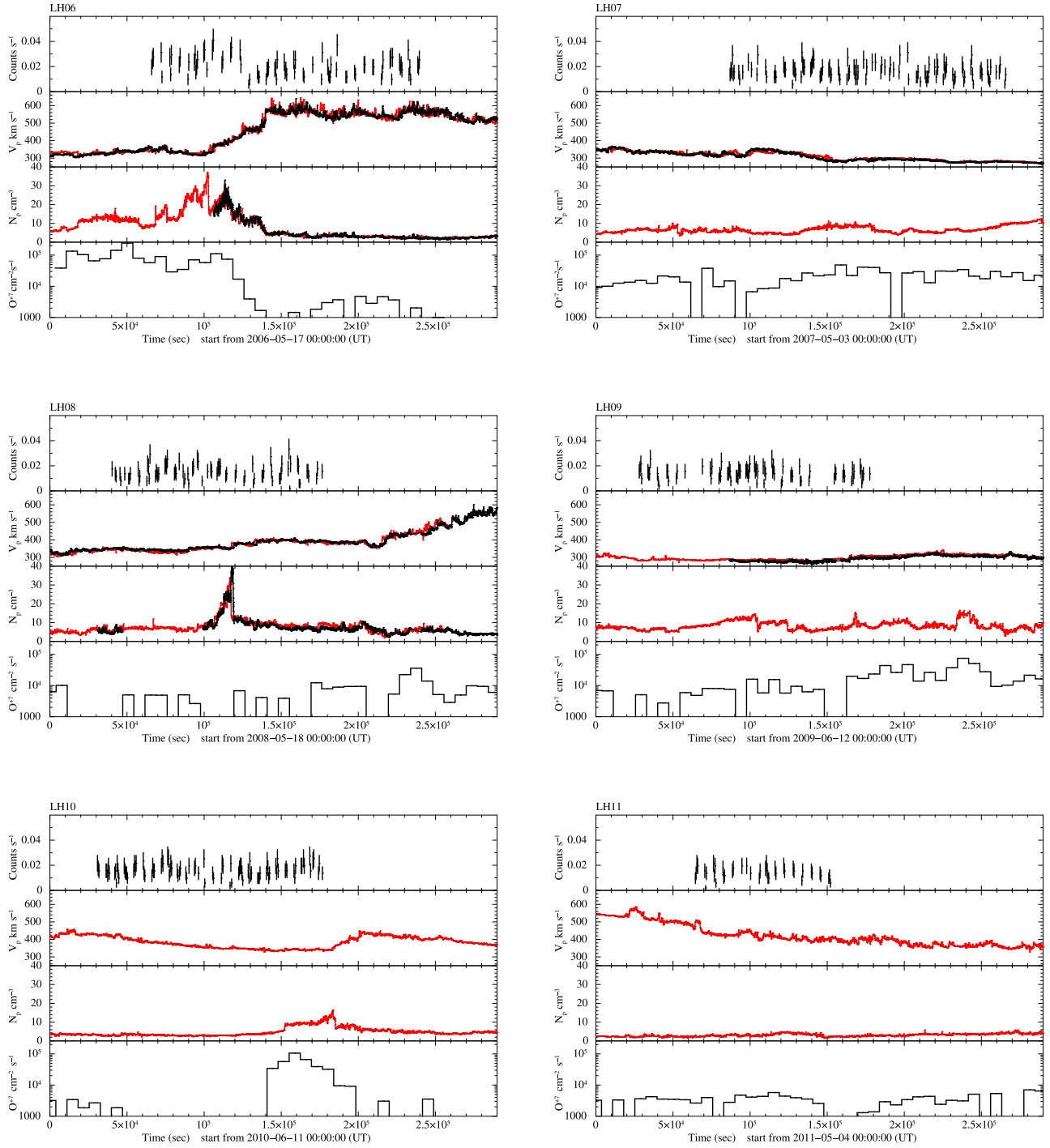


Fig. 1. Correlation between soft X-ray light curves and solar wind parameters during the observations; Suzaku/XIS1 512 s binned 0.5 – 0.7 keV light curve (top), ACE/SWEPAM (black) 64 s and WIND/SWE (red) 96 s time resolution solar wind proton velocity (2nd row), solar wind proton density (3rd row), and ACE/SWICS–SWIMS 2 hour averaged solar wind O^{+7} ion flux (bottom).

penetration depth of solar wind ions to the atmosphere is determined by the interplanetary plasma conditions (Yoshino et al. 2009). Here we explain the specifics of how to determine the data reduction criteria.

First, we checked the solar wind data of monitoring satellites; ACE/SWEPAM¹ or WIND/SWE² for the solar wind protons, and ACE/SWICS–SWIMS³ for the solar wind heavy ions, respectively. The data of ACE/SWICS–SWIMS were only used when the quality flags of solar wind parameters were equal to 0 (meaning “Good quality”). In these observation intervals, there were some missing ACE Level 2 data, for which we compensated with the solar wind proton data measured by WIND. Figure 1 shows the X-ray light curves in the 0.5 – 0.7 keV band, where O VII and O VIII emission lines are dominant, of Suzaku XIS1, the solar wind proton density and velocity with ACE/SWEPAM (black) and WIND/SWE (red), and solar wind O⁺⁷ ion flux with ACE SWICS–SWIMS during each observation. Both ACE and WIND are orbiting around L1 ($\sim 235 R_E$ sunward of Earth), and there is a delay in the solar wind propagation from L1 to the Earth. We shifted the solar wind data by using the velocity averaged over each observation. We compared energy spectra extracted from different intervals sorted by the proton flux in each observation, in order to judge the necessity of screening. Note that the statistical errors in the X-ray light curves are too large to visually identify the influence of geocoronal SWCX.

During LH07, LH09, and LH11, the proton fluxes, expressed as a product of the density and the velocity, were always less than $4.0 \times 10^8 \text{ cm}^{-2}\text{s}^{-1}$. According to the solar wind monitoring at L1, both LH07 and LH09 occurred during slow solar wind conditions, and LH11 was in temporary fast conditions (typical properties of the slow/fast solar winds are summarized in Koutroumpa et al. (2006), Table 1). These were not screened by solar wind flux.

In LH06 and LH10, both proton and ion fluxes were enhanced by the passage of a corotating interaction region (CIR) around the Earth, in which slow solar wind is compressed by fast wind. We compared the O VII line intensities between the CIR passage and the rest of the observation interval. The O VII intensities estimated from spectral fitting (details are described in the next section) were $5.6_{-1.1}^{+1.1}$ (CIR passage) / $2.6_{-0.7}^{+0.8}$ (the rest) LU in LH06, and 7.7 ± 1.3 (CIR passage) / 6.1 ± 1.1 (the rest) LU in LH10, respectively. We used only the data when the solar wind was consistently slow or fast (i.e. from 90 ks after the start of LH06, and within 110 ks from the start of LH10).

Although the proton density data presented a steep increase between 60 ks and 100 ks from the beginning of LH08, there was no enhancement in both the O⁺⁷ flux and O VII. Estimated O VII intensities are $2.7_{-1.3}^{+1.5}$ (60 ks to 100 ks) / $3.0_{-0.9}^{+1.0}$ (the rest) LU respectively. Therefore, we did not screen the LH08 data by the solar wind flux.

¹ http://www.srl.caltech.edu/ACE/ASC/level2/lvl2DATA_SWEPAM.html

² http://web.mit.edu/space/www/wind/wind_data.html

³ http://www.srl.caltech.edu/ACE/ASC/level2/lvl2DATA_SWICS-SWIMS.html

Second, we calculated the structure of the geomagnetic field towards the Suzaku line of sight (LOS) using the Geopack 2008 (Tsyganenko & Sitnov 2005). In all observations, the distance of the Earth–center to the magnetopause (ETM) varied from 1.5 to 15.0 R_E . However, the effect of low ETM distance on the energy spectrum was only confirmed during the passage of a CIR in LH06 that had been already removed. In this analysis, we did not screen the data based on the ETM distance.

3.2. Removal of the Neutral O I $K\alpha$ Line.

We checked the mixing of neutral oxygen lines to the O VII line. Solar X-ray photons scattered with neutral oxygen in Earth’s atmosphere create the O I $K\alpha$ line emission (centroids are $E_{O_2} = 525$ eV and $E_O = 540$ eV). In accordance with previous studies (Smith et al. 2007, Miller et al. 2008, and Yoshino et al. 2009), we calculated the distributions of the neutrals in Earth’s atmosphere using the Normal MSISE–00 model 2001⁴ (Hedin 1991).

The count rate in the 0.5–0.6 keV band increased with the neutral column density only in LH07. We decided to use the X-ray events of LH07 when the neutral oxygen column density was less than 1.0×10^{14} cm⁻² for observation intervals on Earth’s dayside, or 1.0×10^{15} cm⁻² on the nightside. The spectral differences in the 0.5–0.6 keV band were also seen in LH11 when the satellite orbited between the Earth’s day and night side. It is thought to be an effect of the neutral scattering occurring in the atmosphere very close to Suzaku. We only used the LH11 data for spectral analysis when Suzaku was on the nightside.

In addition, a GOES C4.2 class X-ray flare was observed on May 5th 11:00 UT during LH07, and an M2.0 class flare was observed on June 12th 9:00 UT during LH10. However, there was no significant O I $K\alpha$ enhancement in either the Suzaku light curve or the energy spectrum, so we included the data acquired during the flare arrivals.

4. Spectral Analysis

4.1. Response and Background Files

We created a Redistribution Matrix File (RMF) for conversion between the Pulse Invariant (PI) channel spectrum and the energy spectrum, and an Auxiliary Response File (ARF) for the spectral fitting, using the Suzaku FTOOLS software **xisrmfgen** ver. 2009–02–28 and **xissimarfgen** ver. 2010–11–05, respectively (Ishisaki et al. 2007). The emission source of the ARF file is assumed to be a uniform sky with radius of 20’.

A Non X-ray Background (NXB) was constructed using the software **xisnxbgen** ver. 2008–03–08 (Tawa et al. 2008). In order to confirm the reproducibility of **xisnxbgen**, we compared count rates of the calculated NXB with those in each Lockman Hole observation above 12 keV, where the XRT does not reflect X-ray photons. The count rates were consistent

⁴ <http://ccmc.gsfc.nasa.gov/modelweb/atmos/nrlmsise00.html>

within 10%. These results were consistent with other papers (Masui et al. 2009 and Yoshino et al. 2009). To correct the slight difference of the calculated NXB and the observed background, we scaled the normalization of NXB spectrum to equalize its count rate above 12 keV to that of each LH observation.

4.2. Emission Model Description

The purpose of this spectral analysis is to obtain the O VII $K\alpha$ (0.57 keV) and O VIII $Ly\alpha$ (0.65 keV) line intensities precisely, and scrutinize the variability of them among different observations. However, there are some contributions at these line energies from other diffuse emission components that cannot be resolved with the CCD resolution. Therefore, we need to estimate this contribution by using a certain range of energy spectra.

The diffuse emission model consists of three components; the extragalactic unresolved point sources (cosmic X-ray background; CXB), the Galactic halo gas, and a blend of the “local hot bubble” (LHB) and SWCX. The emission of CXB, which is the dominant component in 2–5 keV, is represented by double broken power laws. Their photon indices are $\Gamma = 1.96$ and $\Gamma = 1.54$ below the folding energy at 1.2 keV and $\Gamma = 1.40$ above it. Following Smith et al. (2007), we normalized the broken power law component with photon index of $\Gamma = 1.54$ to 5.7 photons $s^{-1} keV^{-1} sr^{-1}$ at 1 keV. Galactic halo gas, the hot interstellar medium in the Galaxy, is represented by a thin thermal plasma with $kT \sim 0.25$ keV, absorbed by the galactic neutrals (Kuntz & Snowden 2000). The blend of LHB ($\sim 10^6$ K gas surrounding our Solar system) and SWCX is represented by an unabsorbed thin thermal plasma with $kT \sim 0.1$ keV. Though the emission process and fine structures of SWCX induced lines are quite different from a collisional ionization equilibrium (CIE) plasma (Snowden et al. 2009), we treated them as a single CIE plasma in this analysis in accordance with many previous works (Smith et al. 2007, Yoshino et al. 2009, and Henly & Shelton 2010). For the thin thermal plasma emission, the *APEC* model (with AtomDB ver.2.0.1) is applied to estimate both the Galactic halo gas and the LHB+SWCX emissions.

4.3. Spectral Fitting in 0.4–5.5 keV Band

To estimate the oxygen line intensities, we first tried to fit the spectra using a broad energy range from 0.4 to 5.5 keV. Figure 2 shows the Lockman Hole spectra with their best fit double broken power laws + Galactic halo + (LHB + SWCX) models. All six spectra are fitted simultaneously. First, we tried to fit the spectra with the same normalization of CXB for all observations, because their pointing directions were almost the same. The result showed the 90 % confidence ranges of the temperature and the normalized halo all overlapped. Therefore, we decided to take the same value of the halo parameters for all observations. The temperature of the LHB+SWCX blend was fixed at the typical temperature $kT = 0.099$ keV ($\sim 1.15 \times 10^6$ K), derived from observations of the local blank field region, where the contribution of the halo was almost negligible due to the large interstellar absorption (Yoshino et al. 2009, Hagihara et

al. 2010). The best fit values are summarized in the upper 6 rows in Table 2. The reduced χ^2 value is 0.999 for 636 d.o.f., and all spectra were well reproduced by this model.

4.4. Derivation of O VII and O VIII Line Intensities

After determining the model parameters of wide band spectra in §4.3, we tried to fit the same spectra again by fixing the halo temperature at the best fit values, and setting zero oxygen abundances for both the halo and LHB+SWCX, but inserting three Gaussian lines at the O VII $K\alpha$, O VIII $Ly\alpha$, and O VII $K\beta$ energies. As reported in Yoshino et al. (2009), the O VIII $Ly\alpha$ line intensity is weak and the O VII $K\beta$ line at 666 eV cannot be resolved from O VIII $Ly\alpha$. For this reason, it is hard to determine the error of the O VIII $Ly\alpha$ line energy centroid in the Lockman Hole observations. We fixed the centroid of O VII $K\alpha$ at 567 eV, averaging the centroids of resonance (574 eV) and forbidden (561 eV) lines, and the centroids of O VIII $Ly\alpha$ and O VII $K\beta$ at 653 eV and 666 eV respectively. The fraction of the O VII $K\beta$ to O VII $K\alpha$ was also fixed at 8.3% (Kharchenko et al. 2003, Yoshino et al. 2009). The lower 6 rows in Table 2 show the best fit results with this new model, and here we define the intensity of O VII and O VIII lines by normalization of the two inserted Gaussian lines. According to this fitting result, the O VII intensities of the earlier four observations were almost constant within the 90 % statistical error range. However, those of LH10 and LH11 are 2 – 3 LU (= photons $s^{-1}cm^{-2}sr^{-1}$) brighter than the others. The statistical significances of the O VII intensity variation of LH10 and LH11 with respect to an average of LH06 to LH09 (= 2.99 ± 0.38 LU) are 4.5σ (LH10) and 2.3σ (LH11), respectively.

When we use an APEC model with zero O abundance, it is implicitly assumed that the continuum by O atoms is negligible. To confirm that the contribution of the continuum is small, we also fitted the spectra with a thermal plasma model including the continuum by O atoms but no O VII $K\alpha$, O VIII $Ly\alpha$ and O VII $K\beta$ lines, along with three Gaussian lines representing the O emission lines. The normalization of the three Gaussian lines did not change by more than a few %. Hence, we conclude that the contribution of the continuum is small. Note that continuum emission is expected if the origin is a thermal plasma, while no continuum is expected if the origin is SWCX. Our results suggest that the intensity of the three lines can be precisely determined regardless of the continuum assumption, i.e., the origin of the emission.

4.5. Systematic Uncertainties of O VII / O VIII Lines

The absolute intensities of O VII / O VIII lines strongly depend on the X-ray detection efficiency and emission model (Yoshino et al. 2009). First, we checked the uncertainty due to the contaminant thickness on the XIS optical blocking filter. The systematic uncertainty of contaminant thickness is estimated to be $\pm 10\%$ of the nominal value in the CALDB files (Suzaku technical description⁵). We changed the efficiency described in the ARF using the

⁵ <http://www.astro.isas.jaxa.jp/suzaku/doc/suzaku.td/>

software **xiscontamicalc** version 2010–11–05 according to the thickness uncertainty. These systematic errors are smaller than the 90 % statistical ones in Table 2, and we only show the results with the ARF of nominal contamination thickness. If the O VII lines of LH10 and LH11 are equal to the early four observations, the thickness must be overestimated by 50% and 40% of the nominal values in May 2010 and June 2011, respectively (according to the latest CALDB `ae_xi[1-3]_contami_20091201.fits`).

Second, we checked the contribution of the uncertainty of the CXB spectrum below 2 keV to the determination of oxygen line intensities. We tried to use a single power law model with photon index $\Gamma = 1.4$ for the CXB emission instead of double broken power laws. The oxygen lines systematically became 0.3 – 0.4 LU larger than in the case of using the double broken power laws CXB model. However, the differences between them were not dependent on the CXB model.

5. Discussion

From the results of spectral fitting, we found that O VII intensities toward the Lockman Hole were enhanced by 2 – 3 LU in 2010 and 2011, compared to those from 2006 to 2009, during which the intensity was constant within 90% statistical errors. A statistically significant variation of the O VIII line was not detected in our analysis.

As we described in §4.2, O VII emission is considered to arise from three different origins: hot Galactic halo, LHB, and geocoronal/heliospheric SWCX. The emission from the halo and LHB is not time variable on the present observation time scales, and the small difference of the field of view due to azimuthal rotations (20 %) is not likely to produce the observed variation.

The data were screened for enhancements on times of a few tens of ks as much as possible. After this correction, we may consider that most of the geocoronal SWCX is removed. However, enhancements of the heliospheric component due to solar wind ion flux increases in the near-Earth environment (~ 0.5 AU scale) are not removed. Thus we next checked the correlation between the O VII intensity and the solar wind flux averaged over the observation period. The result is shown in Figure 3. During the four Suzaku observations excluding the first and last ones (LH06 and 11), slow solar wind passed around the Earth. The ionization states of ions can be considered to be similar for the four observations (LH07 to LH10). Therefore we can consider that the O^{+7} flux is proportional to the proton flux at least for the four observations. Since the typical elapsed time of the observations is two days, and the typical wind speed is ~ 400 km/s, the lack of positive correlation in Figure 3 suggests that the O VII variation is not correlated with the average ion flux on ~ 0.5 AU scales.

As we discussed in §1, the parallax can produce intensity variations. However, all the observations were made between May 3 and June 13, and we find no correlation between the O VII intensity and the day of year of the observation. Thus the variation is not due to parallax.

We thus consider that the variation is related to variations of the ion flux or the density

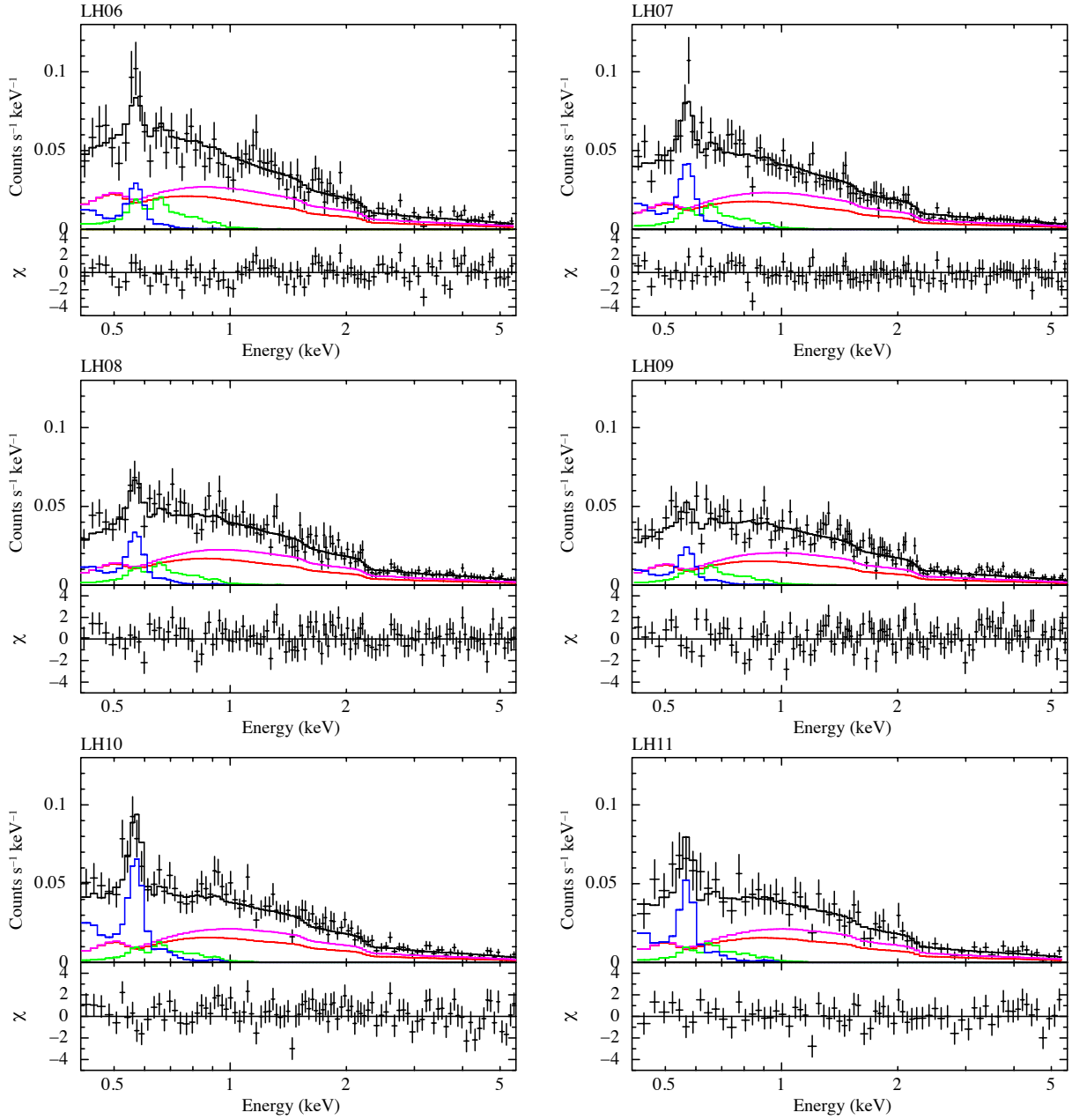


Fig. 2. 0.4 – 5.5 keV Suzaku XIS1 (Back Illuminated CCD) spectra and best fit emission models of the blank field toward the Lockman hole from 2006 to 2011 convolved with the CCD and telescope responses (top panel) and residual of the fit (bottom panel). Black crosses show the observed spectra. Step lines show the best fit models; total (black), Galactic halo (green), LHB+SWCX (blue), CXB with $\Gamma = 1.54$ (magenta), and CXB with $\Gamma = 1.96$ (red) respectively.

Table 2. Results of spectral fitting with double broken power laws CXB + Galactic halo+ (LHB+SWCX) models.

component	CXB		Galactic Halo		LHB+SWCX	O VII	O VIII	$\chi^2/\text{d.o.f.}$
<i>model</i>	<i>phabs*</i> (<i>bknplwls</i> [†])		<i>phabs*</i> (<i>APEC</i>)		<i>APEC</i> [‡]	<i>gaussian</i> [§]	<i>gaussian</i> [§]	
parameter	norm.		norm.		norm.	norm.	norm.	
unit			‡		‡	**	**	
LH06					$9.1^{+4.0}_{-5.3}$	—	—	
LH07					$18.4^{+4.1}_{-5.4}$	—	—	
LH08	4.1 ± 0.2				$17.4^{+4.3}_{-5.5}$	—	—	635.2/636
LH09		$0.216^{+0.025}_{-0.029}$	$1.7^{+1.1}_{-0.4}$		$14.7^{+4.5}_{-5.6}$	—	—	
LH10					$39.7^{+5.7}_{-6.5}$	—	—	
LH11					$31.8^{+8.4}_{-8.9}$	—	—	
LH06					9.0 ± 8.4	2.55 ± 0.74	$0.21 (< 0.62)$	
LH07					20.7 ± 9.7	3.68 ± 0.72	0.61 ± 0.37	
LH08	4.1 ± 0.2				27.5 ± 10.3	3.03 ± 0.77	0.94 ± 0.41	615.9/625
LH09		0.216 (fixed)	2.1 ± 0.8		25.0 ± 10.9	2.69 ± 0.80	0.77 ± 0.42	
LH10					60.1 ± 13.7	6.06 ± 1.07	0.86 ± 0.49	
LH11					42.0 ± 22.5	5.28 ± 1.60	0.97 ± 0.76	

* Absorption column density is fixed at $N_{\text{H}} = 5.8 \times 10^{19} \text{cm}^{-2}$ (Kalberla et al. 2005).

† Normalization of the power law with $\Gamma = 1.54$ is also fixed at 5.7 photons $\text{s}^{-1} \text{cm}^{-2} \text{keV}^{-1} \text{sr}^{-1}$ @1keV.

‡ See details in the text in §4.3.

§ See details in the text in §4.4.

|| The unit of the normalization of a power law component is photons $\text{s}^{-1} \text{cm}^{-2} \text{keV}^{-1} \text{sr}^{-1}$ @1keV.

‡ The emission measure integrated over the line of sight, $(1/4\pi) \int n_e n_{\text{H}} ds$ in the unit of $10^{14} \text{cm}^{-5} \text{sr}^{-1}$.

** The normalization of gaussian component shows the surface brightness whose unit is defined as

L.U. (Line Unit) = photons $\text{s}^{-1} \text{cm}^{-2} \text{sr}^{-1}$.

of neutrals averaged along the line of sight for lengths longer than ~ 0.5 AU. A possible explanation for this is the long term variation of the solar wind properties associated with the solar activity. Based on the number of sunspots, the solar minimum of the Cycle 23 was around December 2008, and then Solar Cycle 24 began. As we described in §1, one of the observational differences between the solar maximum and the minimum is the distributions of the slow and fast solar wind in the solar corona (McComas et al. 2008). The direction of the LH is in the relatively high ecliptic latitude area, at $\beta = 45.2^\circ$, hence the variability of the boundary between the slow and fast winds would affect the O VII intensity.

Figure 4 shows the time dependences of relative sunspot number (NAOJ, private communication with Prof. S. Tsuneta) representing the long term (~ 11 -year) solar cycle together with the present O VII intensities. Solar activities in the northern and southern hemispheres

show different time dependences. The sunspot numbers in the southern hemisphere change symmetrically about the solar minimum, and those in 2006 are almost the same as in 2010 to 2011. On the other hand, the sunspot numbers in northern hemisphere are less than 10 from 2006 to 2010, while they rapidly increase after the minimum and reach 40 in June 2011. The Suzaku line of sight (LOS) points toward the northern hemisphere of the Sun, and here we focus on the solar activity in the northern hemisphere. The figure suggests that the enhancement of O VII emission in 2010 is related to the rapid increase of sunspot number in the northern hemisphere. This unusual situation may be correlated with the north-south asymmetry in Sun's polar magnetic field reported by Hinode (Shiota et al. 2012).

The solar wind distribution maps are obtained by the interplanetary scintillation method (STE lab.⁶). Though the fast wind whose velocity is $>\sim 600 \text{ km s}^{-1}$ extends at high latitudes from 2006 to 2009, the slow solar wind ($<\sim 400 \text{ km s}^{-1}$) actually spreads throughout the northern hemisphere in 2011. If the slow/fast solar wind boundary is at $|\beta| = 20^\circ$ at solar minimum, the line of sight (LOS) of the present observations crosses the boundary and enters into the fast-wind region at $\sim 0.5 \text{ AU}$ from the Earth. Beyond that point, the LOS stays in the fast wind region. On the other hand, if we assume the boundary is at $|\beta| = 50^\circ$ at the solar maximum, the LOS is in the slow wind all the way to the outer boundary of the Heliosphere.

Next, we estimated the SWCX O VII intensity following the model developed by Koutroumpa et al. (2006). In their model, both solar wind ions and interstellar neutrals distribute self-consistently by considering charge exchange loss processes; the density of the solar wind ions basically has an r^{-2} dependence from the Sun, and the densities of interstellar hydrogen and helium were simulated from the so-called classical “hot model” (Lallement et al. 1985). We integrated the heliospheric SWCX emission along the LOS within 90 AU from the Earth. All of the parameters used in this model are same as the Koutroumpa et al. (2006): solar wind proton density is $6.5/3.2 \text{ cm}^{-3}$, velocity $400/750 \text{ km s}^{-1}$, O/H abundance ratio $1/1780 / 1/1550$, and O^{+7} ionization fraction $0.20/0.03$ for the slow/fast wind at 1 AU respectively. In this case, the model predicts O VII line $2.5/1.7 \text{ LU}$ assuming the solar maximum/minimum conditions for the neutral distribution (Note that the increase of O VII intensity is smaller than that expected when we just change the beta angle of fast/slow wind boundary, because the density of neutrals decreases due to strong photoionization by the solar UV photons and charge exchange by the solar wind protons.) Thus this model can explain about one third of the observed O VII intensity variations. There are uncertainties in the solar wind parameters, in particular, of high ecliptic latitude directions. The factor of about three discrepancy may be explained by those uncertainties.

Because the solar wind contains ions other than O^{+7} , the SWCX induced X-ray emission should also contain emission other than O VII. However, those lines were too weak. O VIII emission was positively detected, although its temporal variation was not significantly detected.

⁶ http://stsw1.stelab.nagoya-u.ac.jp/ips_data.html

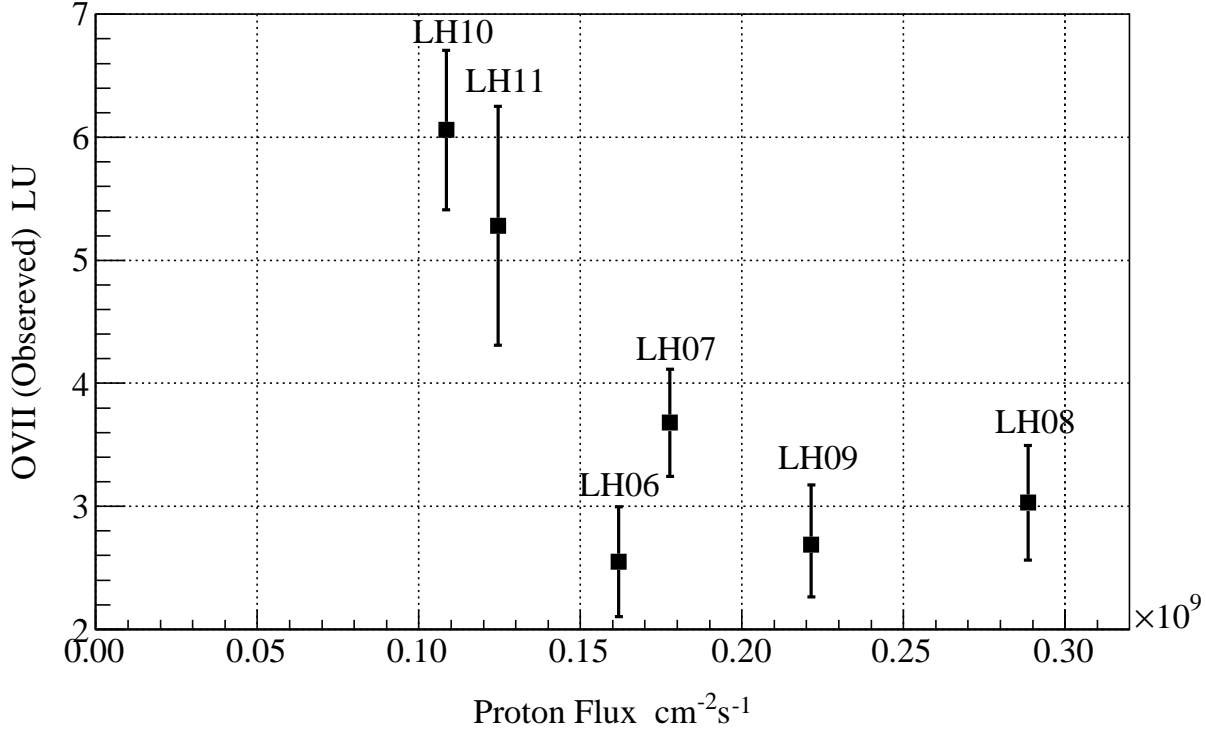


Fig. 3. Comparison of the OVII line intensities obtained from the spectral fitting in Table 2 and solar wind proton flux value. Proton flux was represented by the average of WIND/SWE data during each Suzaku observation.

From the Koutroumpa et al. (2006) maps we estimate that the OVIII line intensity during solar maximum is 0.8 LU and during solar minimum 0.4 LU. The upper limit of the measured OVIII intensity variation (0.75 LU) is consistent with the model predictions.

We are grateful to Dr. Dimitra Koutroumpa for showing us the details of her model and a number of fruitful suggestions as the referee. We also thank to the Suzaku, ACE, and WIND team for providing the data. This work is partly supported by a Grants-in-Aid for Scientific Research from JSPS (Project Number : 09J08405, 21340046 and 22111513).

References

- The Local Bubble and Beyond (Berlin: Springer), 121.
- Dickey, J. M., & Lockman, F. J., 1990, ARA&A, 28, 215.
- Dikpati, M. & Charbonneau, P., 1999, ApJ, 518, 1, 508.
- Fujimoto, R., et al., 2007, PASJ, 59 SP1, S133.
- Hagihara, T., Yao, Y., Yamasaki, N. Y., Mitsuda, K., Wang, Q. D., Takei, Y., Yoshino, T., & McCammon, D., 2010, PASJ, 62, 723.
- Hasinger, G., Burg, R., Giacconi, R., Hartner, G., Schmidt, M., Trumper, J., & Zamorani, G., 1993, A&A, 275, 1.

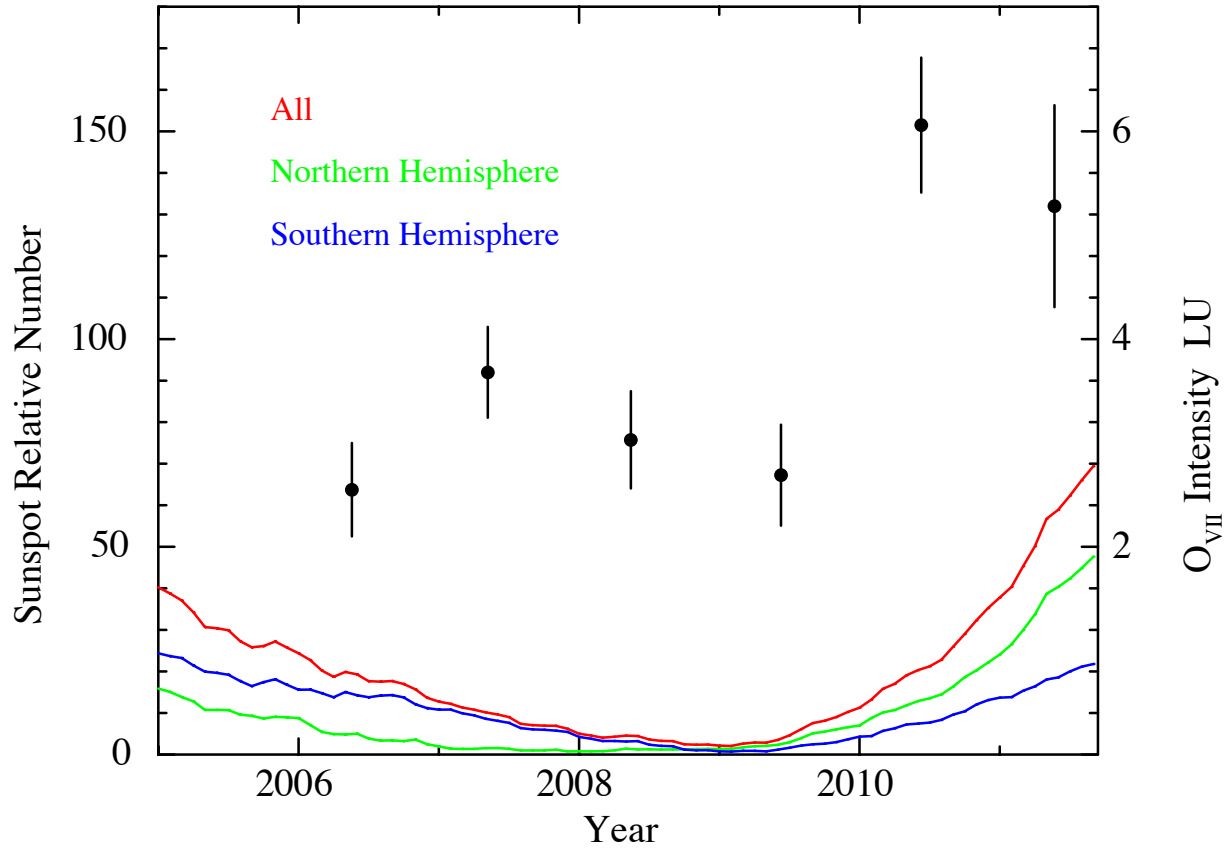


Fig. 4. Time dependences of the NAOJ relative sunspot numbers (red, green, and blue, left y axis) and Suzaku O VII line intensities (black, right one).

Hedin, A. E. 1991, *J. Geophys. Res.*, 96, 1159.

Henley, D. B., & Shelton, R. L., 2010, *ApJS*, 187, 2, 388.

Ishisaki, Y. et al., 2007, *PASJ*, 59 SP1, S113.

Kalberla, P. M. W., Burton, W. B., Hartmann, Dap, Arnal, E. M., Bajaja, E., Morras, R., & Pöppel, W. G. L., 2005, *A&A*, 440, 775.

Kharchenko, V., Rigazio, Matt, Dalgarno, A., & Krasnopolsky, V. A., 2003, *ApJL*, 585, 1, 73.

Koutroumpa, D., Lallement, R., Kharchenko, V., Dalgarno, A., Pepino, R., Izmodenov, V., & Quémerais, E., 2006, *A&A*, 460, 289.

Koutroumpa, D., Acero, F., Lallement, R., Ballet, J., & Kharchenko, V., 2007, *A&A*, 475, 90.

Koutroumpa, D., Smith, R. K., Edgar, R. J., Kuntz, K. D., Plucinsky, P. P. & Snowden, S. L., *ApJ*, 2011, 726, 2, 91.

Koyama, K. et al., 2007, *PASJ*, 59 SP1, S23.

Kuntz, K. D., & Snowden, S. L., 2000, *ApJ*, 543, 1, 195.

Lallement, R., Bertaux, J. L., & Dalaudier, F., 1985, *A&A*, 150, 1, 21.

Lallement, R., Quemerais, E., Bertaux, J. L., Ferron, S., Koutroumpa, D., & Pellinen, R., 2005, *Science*, 307, 1447.

Masui, K., Mitsuda, K., Yamasaki, N. Y., Takei, Y., Kimura, S., Yoshino, T., & McCammon, D., 2009, *PASJ*, 61 SP1, 115.

McCammon, D. et al., 2002, *ApJ*, 576, 1, 188.

McComas, D. J., Ebert, R. W., Elliott, H. A., Goldstein, B. E., Gosling, J. T., Schwadron, N. A., & Skoug, R. M., 2008, *Geophys. Res. Lett.*, 35, 18, L18103.

Miller, E. D. et al., 2008, *PASJ*, 60 SP1, S95.

Mitsuda, K. et al., 2007, *PASJ*, 59 SP1, S1.

Østgaard, N., Mende, S. B., Frey, H. U., Gladstone, G. R., & Lauche, H., 2003, *J. Geophys. Res.*, 108, A7, 18–1.

Pepino, R., Kharchenko, V., Dalgarno, A., & Lallement, R., 2004, *ApJ*, 617, 1347.

Serlemitsos, P. J., et al., 2007, *PASJ*, 59 SP1, S9.

Sfeir, D. M., Lallement, R., Crifo, F., & Welsh, B. Y., 1999, *A&A*, 346, 785.

Shiota, D., Tsuneta, S., Shimojo, M., Sako, N., Suarez, D. O., & Ishikawa, R., 2012, *PASJ*, submitted.

Smith, R. K., et al., 2007, *PASJ*, 59 SP1, S141.

Snowden, S. L., & Freyberg, M. J., 1993, *ApJ*, 404, 403.

Snowden, S. L., Collier, M. R., & Kuntz, K. D., 2004, *ApJ*, 610, 2, 1182.

Snowden, S. L., 2009, *Space Sci. Rev.*, 143, 253.

Tawa, N. et al., 2008, *PASJ*, 60 SP1, S11.

Tsyganenko, N. A., & Sitnov, M. I. 2005, *J. Geophys. Res.*, 110, A03208, doi:10.1029/2004JA010798.

Yoshino, et al., 2009, *PASJ*, 61 805.